



Droplet-on-demand mass spectrometry reveals curvature-dependent interfacial reactivity in aqueous microdroplets

Yu Xia^{a,b}, Xufeng Gao^c, Juan Li^a, Richard N. Zare^{b,1}, Bolei Chen^{d,1}, and Xinxing Zhang^{c,1}

Affiliations are included on p. 6.

Edited by F. Fleming Crim, University of Wisconsin, Madison, WI; received July 21, 2025; accepted October 24, 2025

Water microdroplets offer a chemical environment that can dramatically accelerate reaction rates compared to bulk-phase solutions and even drive chemical transformations not found in bulk solutions. While mass spectrometry has proven indispensable for studying microdroplet chemistry, current methods rely on ensemble-averaged data from polydisperse droplet populations, obscuring the molecular details and droplet-size dependencies of reactions in individual droplets. Here, we present a piezoelectric-driven droplet-on-demand platform that enables direct mass spectrometric analysis of single, size-controlled microdroplets. We demonstrate a broad range of reactions occurring within isolated droplets. These reactions yield products comparable to those generated in conventional spray-based microdroplet systems, confirming that enhanced reactivity is intrinsic to the microdroplet environment. Crucially, we reveal a pronounced droplet-size-dependent reactivity, with smaller droplets exhibiting markedly higher activity per unit surface area. This consistent trend across different reaction types underscores the pivotal role of curvature-modulated interfacial electric fields in governing microdroplet reaction dynamics. Higher electric field strengths cause more radicals to be formed, but these radicals recombine with one another, removing them for reactions with other substrates. Consequently, as our experimental data show, there is an optimum droplet size to yield the highest product reaction rate.

mass spectrometry | single microdroplet | air–water interface | electric field | curvature

Water microdroplet chemistry has garnered wide attention for its ability not only to dramatically accelerate reaction kinetics but also to facilitate chemical transformations that are otherwise thermodynamically unfavorable in bulk solutions (1–3). The high reactivity arises from the unique physical and chemical properties of microdroplets, particularly the spontaneous generation of strong electric fields at the air–water interface of microdroplets, with strengths reaching $\sim 10^9$ V/m (4–6). Such interfacial electric fields can modulate local charge distributions, stabilize high-energy intermediates, align polar molecules, and lower activation barriers for processes involving dipole moment change and electron transfer (7–10). The electric field may result from charge separation at the hydrophilic–hydrophobic interface, the collective aligned orientation of water molecule dipoles on the microdroplet surface, and from the formation of electric double layers (11, 12). Another possible source of the field is the encounter of two oppositely charged droplets (13). Recently, Zare and coworkers found that the droplets generated by pneumatic spraying and acoustic levitation/pressurization include both positively and negatively charged ones (14). Microlightning was observed between oppositely charged microdroplets during separation or approach, generating a local electric field of approximately 3×10^9 V/m (14–16).

On the technique front, spectroscopic methods such as fluorescence and Raman spectroscopy have made valuable contributions to this field by enabling the observation of chemistry that occurs in a single droplet (17–23). These approaches have been instrumental in advancing our understanding of droplet chemical behavior (20, 24–26). However, spectroscopy is often constrained by limited molecular specificity and sensitivity, particularly when detecting short-lived intermediates or structurally similar species (27). Mass spectrometry (MS), with its ability to resolve chemical structures and capture transient species, has been a major tool for the study of microdroplet chemistry (2, 28–33). Yet, the vast majority of MS-based microdroplet studies rely on spray techniques, such as pneumatic nebulization and ultrasonic atomization, that produce continuous, polydisperse droplet streams (34–36). These ensemble approaches inherently average over diverse droplet populations, thereby masking the size-dependent variability and complex interfacial dynamics present in individual droplets. Alternatively stated, current MS methods cannot

Significance

Chemical reactions in aqueous microdroplets are known to proceed at remarkably accelerated rates, yet the decisive factors governing these rate enhancements remain elusive. We introduce a droplet-on-demand mass spectrometry platform that enables real-time analysis of single, size-controlled microdroplets, thereby uncovering how interfacial curvature governs reaction efficiency. Our findings demonstrate that curvature-modulated interfacial electric fields broadly govern droplet-phase chemistry, not only promoting radical-based pathways but also enhancing neutral reactions such as C–N condensation. This work finds that an optimal droplet size exists for maximum reactivity, which depends on the reaction, and establishes curvature as a key parameter in determining interfacial reactivity.

Author contributions: Y.X., R.N.Z., and X.Z. designed research; Y.X., X.G., J.L., B.C., and X.Z. performed research; Y.X. contributed new reagents/analytic tools; Y.X., X.G., J.L., R.N.Z., B.C., and X.Z. analyzed data; and Y.X., R.Z., and X.Z. wrote the paper.

The authors declare no competing interest.

This article is a PNAS Direct Submission.

Copyright © 2025 the Author(s). Published by PNAS. This article is distributed under [Creative Commons Attribution-NonCommercial-NoDerivatives License 4.0 \(CC BY-NC-ND\)](https://creativecommons.org/licenses/by-nc-nd/4.0/).

¹To whom correspondence may be addressed. Email: zare@stanford.edu, blchen@cees.ac.cn or zhangxx@nankai.edu.cn.

This article contains supporting information online at <https://www.pnas.org/lookup/suppl/doi:10.1073/pnas.2519491122/-/DCSupplemental>.

Published December 9, 2025.

tell the difference in reactivity between a single droplet and the encounter of many droplets.

To address these challenges, we developed a piezoelectric-driven droplet-on-demand (DOD) platform capable of generating single aqueous microdroplets with precisely controlled diameters and adjustable frequencies of delivery. DOD technology has a history of several decades in applications such as inkjet printing and microfluidics (37, 38), and numerous studies have also employed single droplets as microreactors to investigate redox processes. (39–42) Here, we advance this concept by directly coupling single-droplet generation with MS, enabling real-time molecular characterization. As the droplets are delivered without contacting capillary surfaces or experiencing auxiliary fields, the system inherently avoids the secondary activation that can occur in other instrumental arrangements (43), allowing the measured reactivity to originate from the droplets themselves. With this method, we directly observed a broad array of chemical reactions occurring within isolated droplets, demonstrating that such reactivity is intrinsic to individual droplets rather than an emergent ensemble effect. We also uncovered reproducible size-dependent and curvature-dependent trends in the reactivity, small droplets yielded higher reactivity unless other competing side reactions existed. These observations demonstrate that within microdroplet reactors fabricated from ultrapure water, droplet size, and curvature effectively modulate the interfacial electric field strength, thereby influencing the resultant reaction rates. Altogether, our findings not only expand the mechanistic understanding of the air–water interfacial chemistry on a single droplet but also establish a powerful tool for probing chemical reactivity at the single-droplet level. This approach provides a well-defined platform for investigating curvature-dependent interfacial reactivity in microscale systems, offering insights that may inform future applications in synthetic chemistry, chemical analysis, and interfacial catalysis.

Materials and Methods

As illustrated in Fig. 1A, our DOD device consists of a piezoelectric actuator coupled to a precision-guided needle assembly and a microfabricated droplet outlet precisely aligned with the mass spectrometer inlet.

A sinusoidal electrical signal applied to the piezoelectric ceramic element drives horizontal displacement of a stainless-steel plunger, which expels single droplets through a narrow nozzle. Droplets generated by this method traverse the distance to the mass spectrometer inlet in about 5 to 10 ms under ambient conditions (Fig. 1B). It is evident from Movies S1 and S2 that the single droplet did not contact the MS capillary, ruling out the possibility that the contact will energize the droplet (43). As illustrated in Fig. 1C, droplet diameter, typically 5 to 150 μm , scales linearly with the applied piezoelectric driving voltage (Fig. 1C and Movie S2). By adjusting the frequency of the input signal, we can achieve stable temporal spacing between droplets on the order of seconds. Fig. 1D shows mass spectral signal strengths from each droplet injection repeated every 3 s, and each spike represents the detection of one droplet.

Unlike conventional continuous spray methods such as electrospray or pneumatic nebulization, which produce a cloud of droplets and time-averaged mass spectra, our method utilizes the inverse piezoelectric effect of high-speed piezoelectric ceramic to mechanically generate discrete droplets. This approach enables temporal resolution and well-defined droplet compositions. Additionally, our technique operates without applied voltages, surfactants, or nebulizing gases, thereby preserving native interfacial properties. Consequently, this system enables direct assessment of chemical reactions within individual droplets in a precisely controlled and reproducible manner.

Results and Discussion

To assess the intrinsic and general nature of this reactivity, we surveyed 16 benchmark reactions spanning radical formation, oxidation, reduction, and C–N bond construction, each occurring within an isolated, size-defined droplet (SI Appendix, Table S1 and Figs. S1–S16). It is known that aqueous microdroplet chemistry occurs at and near the interface. While total product intensities naturally increase with surface area, our results reveal that normalization by surface area uncovers a clear size-dependent trend. This demonstrates that curvature, rather than surface area alone, plays an independent role in controlling interfacial reactivity. As will be shown in what follows, this is not a fully correct way to understand what is controlling droplet reactivity and fails to appreciate the importance of the droplet's curvature.

To investigate how curvature modulates interfacial chemical reactivity in aqueous microdroplets, we leveraged the DOD platform to

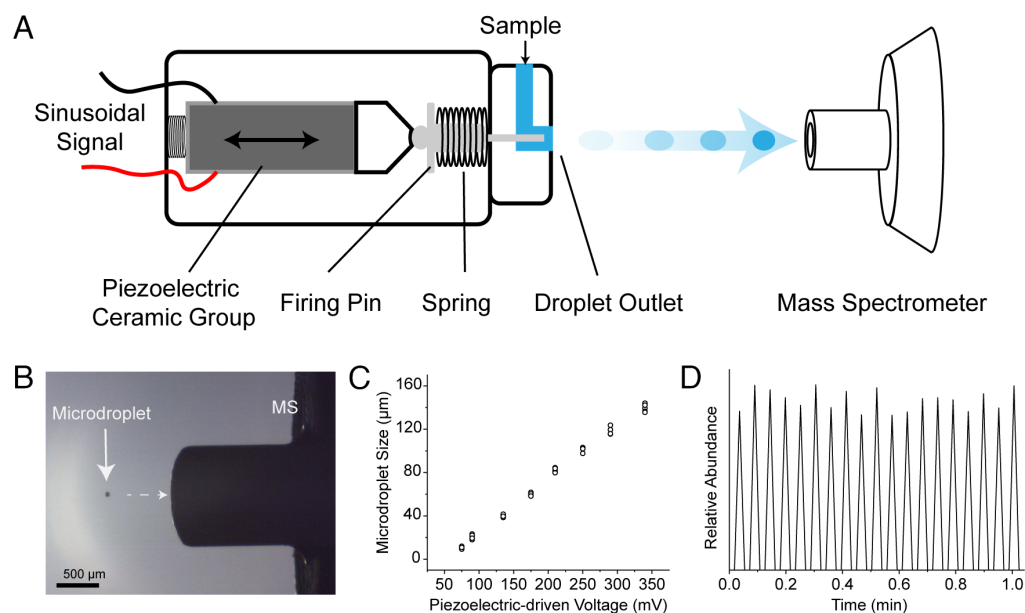


Fig. 1. Schematic and operation of the single-droplet MS platform. (A) Schematic illustration of the piezoelectric DOD system coupled with a mass spectrometer. (B) High-speed imaging showing the generation and trajectory of a single droplet entering the MS inlet. (C) Relationship between applied voltage and droplet diameter, demonstrating precise size control from 5 to 150 μm . (D) Continuous and stable mass spectrometric signals obtained from successive single-droplet injections at 3-s intervals over 1 min.

generate single droplets with precisely controlled diameters ranging from 5 to 150 μm . Compared to polydisperse spray-based methods, this system enables high-resolution probing of droplet-specific behavior while preserving the native air–water interface. Across multiple reaction classes—including oxidation, reduction, radical formation, and bond formation—we observed a general trend: Smaller droplets tended to exhibit higher reactivity per droplet. In certain systems, reactivity diminished or plateaued at the smallest sizes, likely resulting from competing quenching or decomposition pathways.

Smaller droplets possess higher interfacial curvature, which strengthens the electric field at the air–water boundary. To rationalize this effect, we employed a simplified Poisson–Boltzmann treatment (see *SI Appendix* for derivation), yielding an analytic expression in which the surface electric field consists of a constant term plus a curvature-dependent contribution:

$$E(R) = \psi(\text{surface}) \left(\kappa + \frac{1}{R} \right), \quad [1]$$

where $\psi(\text{surface})$ is the diffuse-layer potential at the droplet interface, κ is the inverse Debye length, and R is the droplet radius. Thus, curvature introduces an additional $1/R$ term, consistent with the observed size dependence. Under our experimental conditions with ultrapure water, $\kappa R \gg 1$, meaning curvature acts as a finite but nonnegligible correction that becomes most pronounced for the smallest droplets. When electrolytes are added, the Debye length contracts relative to R , suppressing curvature

effects and approaching the planar limit. Accordingly, enhanced reactivity in small droplets arises from curvature-amplified interfacial electric fields, whereas larger droplets exhibit weaker fields and reduced intrinsic reactivity.

Consistent with this prediction, increasing ionic strength progressively reduces reactive oxygen species (ROS) formation (*SI Appendix, Fig. S17*). Ultrapure-water droplets exhibit the highest reactivity, which decreases in dilute NaCl solutions and approaches the level of natural seawater, whereas bulk water shows negligible activity. This Debye-length–mediated suppression further confirms that curvature-enhanced interfacial fields govern droplet reactivity under low-ionic-strength conditions. Accordingly, enhanced reactivity in small droplets arises from curvature-amplified interfacial electric fields, whereas larger droplets exhibit weaker fields and reduced intrinsic reactivity.

In what follows, we examine the experimental findings that the drop-on-demand MS measurements have achieved. The Schiff base condensation (44) represents a neutral molecular coupling reaction that proceeds through nucleophilic addition and subsequent dehydration, without the involvement of radical or electron intermediates. As illustrated in Fig. 2A, benzaldehyde (BA) reacts with aniline (AN) at the air–water interface to yield the imine product (M), detected as a protonated ion at m/z 182. The mass spectrum of a single droplet (Fig. 2B) clearly shows this product peak alongside the reactant ions at m/z 94 ($\text{AN}+\text{H}$)⁺ and several adducts and intermediates at m/z 111 and 135. Despite its non-redox nature, the condensation reaction still exhibits strong

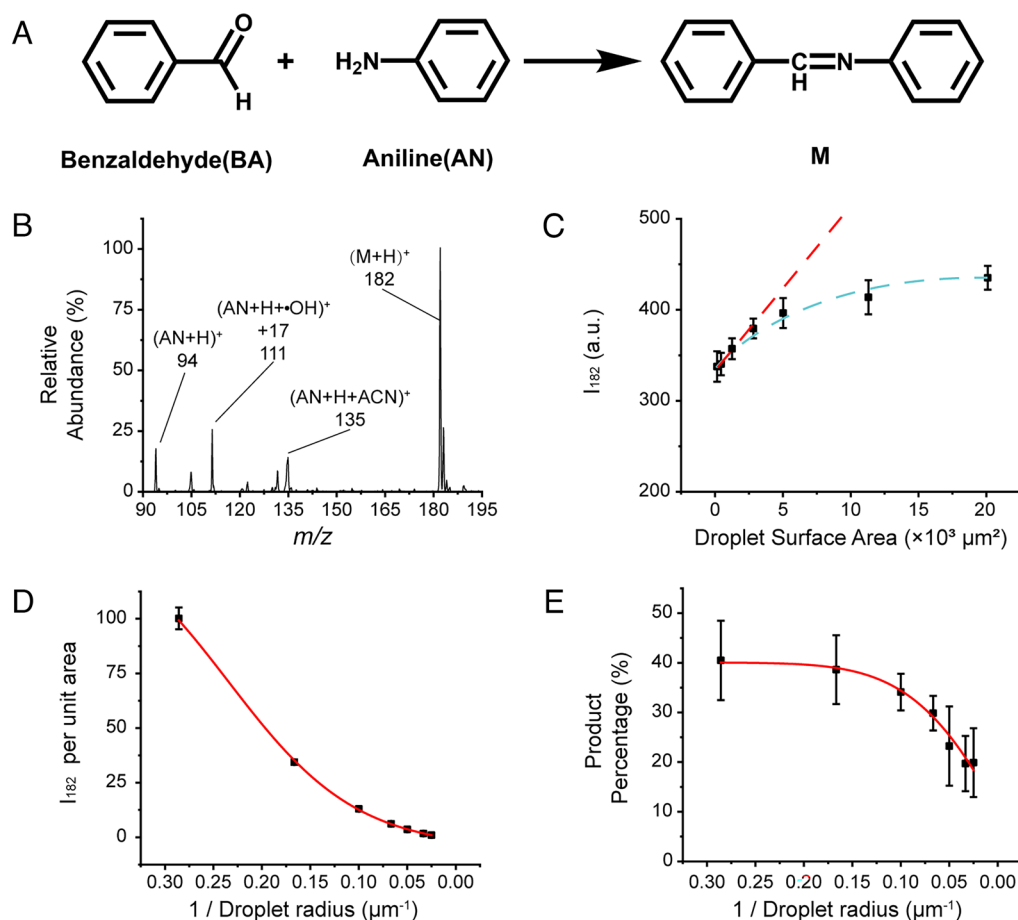


Fig. 2. MS study of Schiff base formation in microdroplets with varying curvature. (A) Reaction scheme. (B) Mass spectrum showing the imine product (M) at m/z 182 formed by condensation of benzaldehyde (BA) and aniline (AN) within single droplets. (C) Intensity (I_{182}) of the product ion m/z 182 measured from droplets with different surface areas. The dashed red line represents the expected behavior if droplet reactivity scaled with droplet surface area. (D) Surface-area-normalized intensity (I_{182}/A) as a function of inverse droplet radius. (E) Product yield as a function of inverse droplet radius.

curvature dependence. As shown in Fig. 2C, I_{182} increases with the droplet surface area ($A = 4\pi r^2$). Because the reaction occurs at the air–water interface, this increase primarily reflects the larger surface area rather than higher interfacial reactivity. To clarify whether this increase is solely due to the expanded surface area or also involves curvature-dependent interfacial effects, we compared the observed I_{182} growth trend (blue dashed line) with a projected linear growth (red dashed line) that would be expected if surface area were the only factor influencing reactivity. The deviation between these two trends highlights that the increase in I_{182} is sublinear, implying that smaller droplets are intrinsically more reactive per unit area than larger ones. Therefore, I_{182} was normalized by the droplet surface area to better quantify reactivity per unit interface. The resulting normalized intensity (I_{182}/A), plotted in Fig. 2B, reveals a clear monotonic decrease with increasing droplet radius which is proportional to curvature. This result is predicted by the simple model we have presented above (Eq. 1).

We propose that the interfacial electric field plays a direct and facilitating role in the Schiff base condensation process. As curvature increases, the associated interfacial electric field becomes stronger, promoting molecular polarization and orientational alignment of the reactants at the air–water boundary. These field-enhanced effects increase the probability of productive collisions and stabilize dipolar transition states, thereby accelerating the formation of the C=N bond. The reaction product yield, shown in Fig. 2E, decreases monotonically with decreasing curvature (i.e., with increasing droplet size), confirming that smaller, more curved droplets exhibit higher intrinsic reactivity. Unlike redox processes that may be complicated by competing radical or electron consumption pathways, this neutral condensation reaction proceeds cleanly at the interface, allowing the curvature dependence to be observed without ambiguity. The precise physical origin of this effect remains open, and possible contributors include variation of interfacial thickness with curvature or other structural features of the air–water boundary. Nevertheless, the consistent size dependence provides a clear and reproducible delineation of the curvature effect. These results reinforce the broader principle that curvature-induced interfacial electric fields can promote diverse chemical transformations, including neutral pathways that do not involve charged or radical intermediates.

Theoretically, the curvature effect has a significant impact on the generation of interfacial free radicals. Therefore, we use m/z 36 as a marker to assess the curvature-size dependence of hydroxyl radical formation, which corresponds to a hydroxyl radical combined with a hydronium cation through hydrogen bonding ($\bullet\text{OH}\text{--}\text{H}_3\text{O}^+$) (45–48). As shown in *SI Appendix*, Fig. S1, the

mass spectrum of a single droplet exhibits a clear peak at m/z 36 (47). The intensity of m/z 36 (denoted as I_{36}) reflects the abundance of hydroxyl radicals and thus serves as an indicator of oxidative activity. As shown in Fig. 3A, the absolute intensity of I_{36} increases with droplet size, consistent with the larger total surface area available for hydroxyl radical formation. However, the observed increase is sublinear compared to the projected linear trend expected if surface area were the sole governing factor. This deviation indicates that smaller droplets exhibit enhanced intrinsic reactivity per unit area. To capture this effect, we normalized I_{36} by surface area (I_{36}/A), which reveals a clear monotonic decrease with increasing droplet radius (Fig. 3B), demonstrating the predicted curvature dependence. This trend confirms that smaller-radius droplets produce more hydroxyl radicals per unit surface area and suggests that the interfacial electric field is amplified by curvature, enhancing local redox activity beyond what would be expected from surface area alone. To demonstrate the unprocessed trend, *SI Appendix*, Fig. S18 shows the absolute signal intensity as a function of droplet size, confirming an overall increase with increasing diameter.

In the melatonin oxidation reaction (*SI Appendix*, Fig. S2), the primary product at m/z 250 arises from the direct addition of hydroxyl radicals to the indole ring of melatonin (47). The absolute intensity of this product ion, m/z 250 (I_{250}), increases gradually with the surface area of the droplet, but the rate of growth slows down (Fig. 4A). However, after normalization to the surface area, the area-specific signal (I_{250}/A) reveals a pronounced curvature dependence (Fig. 4B), with significantly higher product formation per unit interface in smaller, more curved droplets. This result parallels the trend observed in Fig. 3 and confirms that melatonin oxidation is more efficient as a function of droplet curvature.

However, when overall product yield is considered—calculated as the percentage of melatonin oxidized relative to total detected species (Fig. 4C)—a nonmonotonic trend emerges. The product yield increases with curvature up to a maximum near 30 μm diameter, then decreases for smaller sizes. We observe a bell-shaped dependence of product yield on curvature, which we attribute to a balance between field-enhanced radical generation and competing side processes. Hydroxyl radicals ($\bullet\text{OH}$), spontaneously generated at the air–water interface through field-driven mechanisms, can either react productively with melatonin or undergo bimolecular recombination to form H_2O_2 . Additional pathways, such as electron capture by ambient O_2 , CO_2 , or NO_2 , may also contribute to reducing $\bullet\text{OH}$ availability. As curvature increases, the interfacial field strength rises, enhancing $\bullet\text{OH}$ generation.

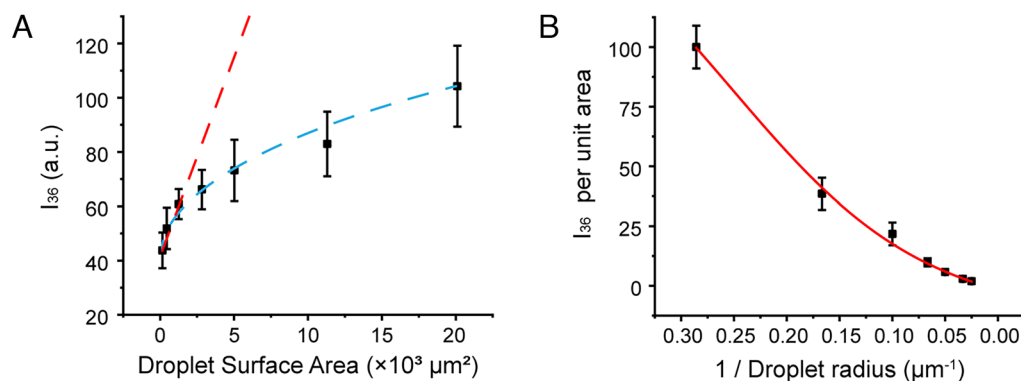


Fig. 3. Curvature-dependent hydroxyl radical signal intensity in single aqueous microdroplets. (A) Intensities of m/z 36 (I_{36}) measured from droplets of different surface areas. The dashed red line represents the expected behavior if droplet reactivity scaled with droplet surface area. (B) Surface-area-normalized intensities of m/z 36 ($I_{36}/A_{\text{droplet}}$) as a function of inverse droplet radius.

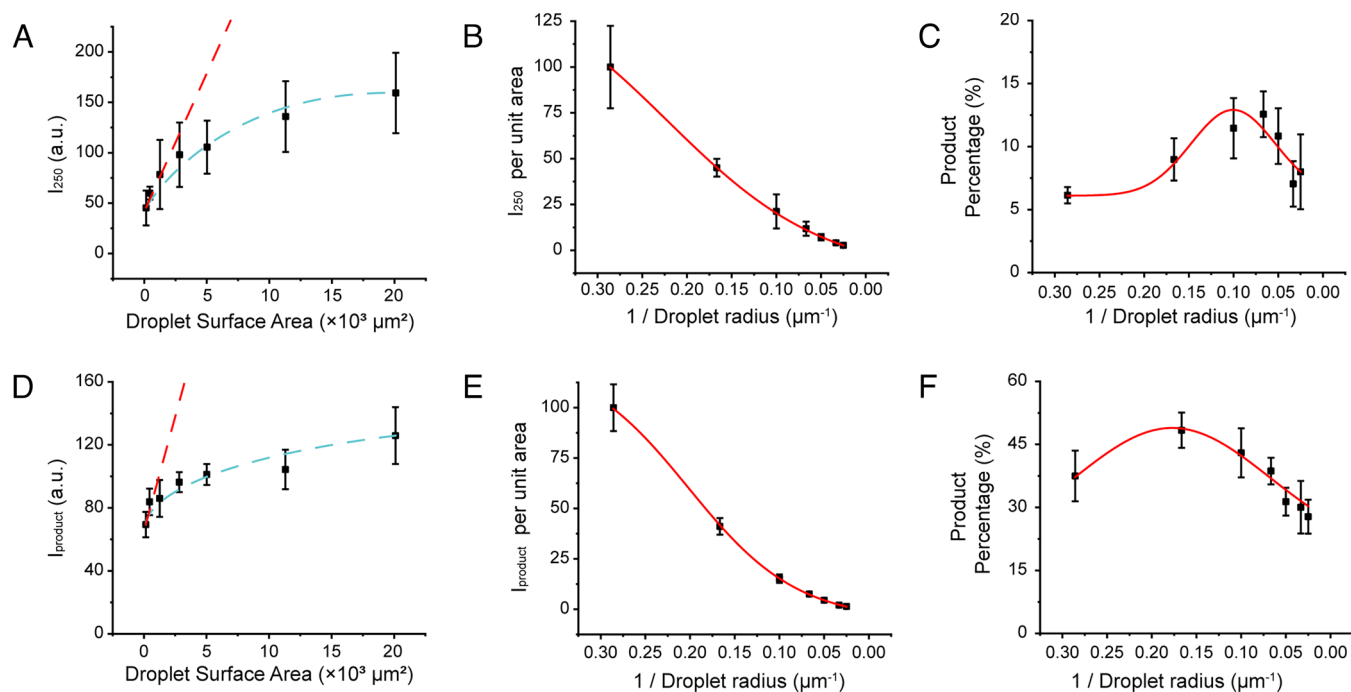


Fig. 4. MS study of redox reactions in different curvature microdroplets. (A) *Melatonin (MLT) oxidation*. Intensity (I_{250}) of m/z 250 measured from droplets of different surface areas. The dashed red line represents the expected behavior if droplet reactivity scaled with droplet surface area. (B) Surface-area-normalized intensity of m/z 250 ($I_{250}/A_{\text{droplet}}$) as a function of inverse droplet radius. (C) Yield of the oxidation product as a function of inverse droplet radius. (D) *Methyl viologen (MV) reduction*. Intensities of productions ($I_{171} + I_{185} + I_{186}$) measured from droplets of different surface areas. The dashed red line represents the expected behavior if droplet reactivity scaled with droplet surface area. (E) Surface-area-normalized intensities of productions as a function of inverse droplet radius. (F) Yield of the reduction product as a function of inverse droplet radius.

However, beyond a critical field strength or radical density, these side processes become increasingly dominant, lowering the net yield of melatonin oxidation. This interplay between field-enhanced reactivity and curvature-induced loss highlights the existence of an optimal droplet size regime for maximizing reactivity.

The reduction of methyl viologen (MV^{2+}) to its radical cation form (MV^+ , m/z 186) represents an interfacial single-electron transfer process that also exhibits strong curvature dependence. As shown in *SI Appendix, Fig. S7A*, the mass spectrum of a single droplet contains the parent ion at m/z 93 (MV^{2+}), the reduced product MV^+ at m/z 186, and secondary fragment ions at m/z 171 and 185, likely resulting from MV^+ decomposition (*SI Appendix, Fig. S7B*) (49). The total product signal (I_{product})—calculated as the summed intensities of m/z 171, 185, and 186—shows a nonlinear increase (gradually slowing down) with droplet surface area (Fig. 4D), consistent with a surface-mediated process. However, after normalization to droplet surface area, the area-specific intensity (I_{product}/A) reveals a pronounced decrease with increasing droplet radius (Fig. 4E), confirming that smaller droplets support higher intrinsic reactivity per unit interface.

Interestingly, the product yield, calculated as the percentage of reduced products relative to total MV, exhibits a bell-shaped dependence on droplet curvature, peaking near 15 μm diameter (Fig. 4F). This nonmonotonic trend mirrors that of melatonin oxidation and underscores the dynamic balance between interfacial activation and competing side reactions. In this case, curvature-induced electric fields promote interfacial electron accumulation, facilitating the reduction of MV^{2+} to MV^+ . However, as interfacial electron density increases in highly curved droplets, competing reductive pathways become significant. Electrons may be consumed by atmospheric species such as protons, O_2 , NO_2 , and CO_2 in ambient air, forming O_2^- , NO_2^- , and HCO_3^- , respectively (50). These processes divert electrons away from the primary redox pathway, ultimately decreasing MV^+ yield at the smallest

droplet sizes despite their elevated field strength. Together, these results reinforce the central mechanistic role of curvature in modulating interfacial electron dynamics. Curvature-enhanced electric fields can strongly promote redox reactivity, but only up to a point—beyond which increased carrier density also activates competing sinks. The observed product yield maximum therefore reflects an optimal balance between electric-field-enhanced reactivity and side-reaction suppression.

While the curvature-induced electric field accounts for the intrinsic reactivity of single droplets, additional electrostatic contributions may emerge in systems containing multiple droplets in close proximity. To explore this possibility, we compared the oxidation of caffeine under single-droplet DOD conditions and under conventional pneumatic spraying, keeping all other parameters constant (i.e., droplet size, reactant concentration, and instrumental settings; see *SI Appendix, Fig. S19*). Notably, the spray-based system produced significantly higher product ion signals. We attribute this enhancement to collective electrostatic interactions between neighboring droplets, which may give rise to localized interdroplet electric fields absent in isolated droplets. These interactions could further polarize the interface or assist in charge redistribution, effectively amplifying the chemical potential of the microdroplet ensemble. This observation highlights a secondary mechanism of field enhancement, arising from droplet–droplet coupling, that operates in dense sprays but is absent in isolated droplet systems.

Although the reactions investigated span a broad range of mechanistic classes—including radical-mediated oxidation, interfacial electron transfer, and neutral molecular addition—the underlying physical driver of their size- and curvature-dependent reactivity is unified. Smaller droplets, by virtue of their higher curvature, generate stronger interfacial electric fields that enhance charge separation, molecular polarization, and interfacial organization, collectively leading to increased reaction efficiency per unit surface

area. In contrast, larger droplets exhibit weaker fields and correspondingly lower interfacial reactivity. This consistent trend across fundamentally different reaction types underscores the central role of curvature-modulated electrostatics in dictating microdroplet chemistry. Notably, even reactions that do not involve charged or radical intermediates remain highly sensitive to the local interfacial field environment, highlighting the broad and unifying influence of curvature-enhanced electric fields on droplet-phase reactivity.

Conclusions

In summary, we have developed a piezoelectric-driven DOD platform that enables direct mass spectrometric interrogation of chemical reactions within individual aqueous microdroplets. This approach overcomes the limitations of ensemble-averaged spray techniques by providing real-time, high-resolution detection of transient intermediates and mechanistic signatures at the single-droplet level. Using this platform, we demonstrated a diverse set of spontaneous redox processes, radical-mediated transformations, and C–N bond-forming reactions occurring in isolated droplets under ambient conditions. Systematic size-controlled studies revealed that droplet curvature—rather than size alone—plays a pivotal role in governing interfacial reactivity. We established a quantitative relationship between droplet radius and interfacial electric field strength, showing that higher curvature amplifies the electric field at the air–water interface, thereby enhancing charge separation, radical formation, and reaction rates. Notably, distinct reactivity regimes emerged across different droplet sizes, shaped by the balance between field-driven activation and competing side reactions. Comparative experiments further revealed that dense droplet ensembles can generate collective electrostatic effects

beyond those of single droplets, pointing to a new layer of reactivity enhancement via interdroplet interactions. Together, these findings establish a tool for mechanistic investigations of microdroplet chemistry, offering new opportunities for the rational design and control of interfacial reactions in synthetic chemistry, environmental systems, and microscale catalysis.

Data, Materials, and Software Availability. All study data are included in the article, the [supporting information](#), and the publicly available link: <https://github.com/YuXia19/Droplet-on-Demand-Mass-Spectrometry> (51).

ACKNOWLEDGMENTS. X.Z. acknowledges the National Key R&D Program of China (2023YFE0124200), the National Natural Science Foundation of China (22325402&22174073), the Natural Science Foundation of Tianjin City (21JCJQC00010), the Nankai Cangzhou Chemistry fund (NCC2022PY05), the Haihe Laboratory of Sustainable Chemical Transformations, and the Frontiers Science Center for New Organic Matter at Nankai University (63181206). Y.X. acknowledges the National Natural Science Foundation of China (22306073), the Hubei Provincial Department of Education Scientific Research Project (Q20234408). B.C. acknowledges the National Natural Science Foundation of China (22376080), and the Hubei Provincial Natural Science Foundation of China (2024AFA089). R.N.Z. acknowledges the US Air Force Office of Scientific Research through the Multidisciplinary University Research Initiative program (AFOSR FA9550-21-1-0170).

Author affiliations: ^aHubei Key Laboratory of Environmental and Health Effects of Persistent Toxic Substances, School of Environment and Health, Jiangnan University, Wuhan 430056, China; ^bDepartment of Chemistry, Stanford University, Stanford, CA 94305; ^cCollege of Chemistry, State Key Laboratory of Advanced Chemical Power Sources, Tianjin Key Laboratory of Biosensing and Molecular Recognition, Frontiers Science Centre for New Organic Matter, Nankai University, Tianjin 300071, China; and ^dState Key Laboratory of Environmental Chemistry and Toxicology, Research Center for Environmental Sciences, Chinese Academy of Sciences, Beijing 100085, China

1. Z. Wei, Y. Li, R. Graham Cooks, X. Yan, Accelerated reaction kinetics in microdroplets: Overview and recent developments. *Annu. Rev. Phys. Chem.* **71**, 31–51 (2020).
2. X. Yan, R. M. Bain, R. Graham Cooks, Organic reactions in microdroplets: Reaction acceleration revealed by mass spectrometry. *Angew. Chem. Int. Ed.* **55**, 12960–12972 (2016).
3. S. Jin *et al.*, The spontaneous electron-mediated redox processes on sprayed water microdroplets. *JACS Au* **3**, 1563–1571 (2023).
4. R. Lixue Shi *et al.*, Water structure and electric fields at the interface of oil droplets. *Nature* **640**, 87–93 (2025).
5. H. Xiong, J. K. Lee, R. N. Zare, W. Min, Strong electric field observed at the interface of aqueous microdroplets. *J. Phys. Chem. Lett.* **11**, 7423–7428 (2020).
6. H. Hao, I. Leven, T. Head-Gordon, Can electric fields drive chemistry for an aqueous microdroplet? *Nat. Commun.* **13**, 280 (2022).
7. A. J. Colussi, Mechanism of hydrogen peroxide formation on sprayed water microdroplets. *J. Am. Chem. Soc.* **145**, 16315–16317 (2023).
8. P. Skurski, J. Simons, Two potential paths for OH radical formation on surfaces of pure water microdroplets. *J. Chem. Phys.* **160**, 034708 (2024).
9. H. Xiong, J. K. Lee, R. N. Zare, W. Min, Strong concentration enhancement of molecules at the interface of aqueous microdroplets. *J. Phys. Chem. B* **124**, 9938–9944 (2020).
10. A. C. Aragonès *et al.*, Electrostatic catalysis of a Diels–Alder reaction. *Nature* **531**, 88–91 (2016).
11. C. F. Chamberlayne, R. N. Zare, Simple model for the electric field and spatial distribution of ions in a microdroplet. *J. Chem. Phys.* **152**, 184702 (2020).
12. S. Shaik, D. Danovich, S. Kalita, K. D. Dubey, Oriented electric fields—Universal catalysts. *Acc. Chem. Res.* **58**, 3071–3080 (2025).
13. Y. Xia *et al.*, Visualization of the charging of water droplets sprayed into air. *J. Phys. Chem. A* **128**, 5684–5690 (2024).
14. Y. Meng, Y. Xia, J. Xu, R. N. Zare, Spraying of water microdroplets forms luminescence and causes chemical reactions in surrounding gas. *Sci. Adv.* **11**, ead8979 (2025).
15. Y. Meng, E. Gnanamani, R. N. Zare, Water droplet microlightning sparks alkyne ozonolysis. *J. Am. Chem. Soc.* **147**, 23399–23404 (2025).
16. J. Zhou *et al.*, Charged water microdroplets enable dissociation of surrounding dioxygen. *J. Am. Chem. Soc.* **147**, 10916–10924 (2025).
17. T. Fukuda *et al.*, Real-time monitoring of chemical reaction in microdroplet using fluorescence spectroscopy. *Sens. Actuators B Chem.* **203**, 536–542 (2014).
18. A. Bierstedt, C. Warschat, Y. You, K. Rurack, J. Riedel, Stimulated raman scattering by intracavity mixing of nanosecond laser excitation and fluorescence in acoustically levitated droplets. *Anal. Methods* **12**, 5046–5054 (2020).
19. Y. Zheng *et al.*, Absorption-based rapid acquisition of single-molecule kinetics from unstable enzymes in microdroplets. *Small* **20**, 2309463 (2024).
20. Y. Yu *et al.*, Acoustic wave-driven microdroplet enrichment for surface-enhanced Raman spectroscopy detection. *Optics Express* **3**, 364–377 (2024).
21. M. I. Jacobs, E. T. Aleman, R. G. Zepeda, Confocal fluorescence imaging of levitated particles and microdroplets. *Aerosol Sci. Technol.* **59**, 833–844 (2025).
22. R. Allen LaCour, J. P. Heindel, R. Zhao, T. Head-Gordon, The role of interfaces and charge for chemical reactivity in microdroplets. *J. Am. Chem. Soc.* **147**, 6299–6317 (2025).
23. M. Sano, K. Kamei, T. Yatsuhashi, K. Sakota, Localization and orientation of dye molecules at the surface of a levitated microdroplet in air revealed by whispering gallery mode resonances. *J. Phys. Chem. Lett.* **15**, 8133–8141 (2024).
24. W. Wang *et al.*, Significantly accelerated photoactivated formation of atmospheric sulfate at the air–water interface of microdroplets. *J. Am. Chem. Soc.* **146**, 6580–6590 (2024).
25. Y. Liu *et al.*, Unveiling the role of carbonate radical anions in dust-driven SO₂ oxidation. *J. Geophys. Res.: Atmos.* **129**, e2023JD040017 (2024).
26. E. Kočíšová, A. Žbeta Kůřilová, M. Procházka, Analytical applications of droplet deposition Raman spectroscopy. *Analyst* **149**, 3276–3287 (2024).
27. K. R. Wilson, A. M. Prophet, Chemical kinetics in microdroplets. *Annu. Rev. Phys. Chem.* **75**, 185–208 (2024).
28. H. Kafeenah, H.–H. Jen, S.–H. Chen, Microdroplet mass spectrometry: Accelerating reaction and application. *Electrophoresis* **43**, 74–81 (2022).
29. Y. Xin, Emerging microdroplet chemistry for synthesis and analysis. *Int. J. Mass Spectrom.* **468**, 116639 (2021).
30. J. K. Lee, S. Kim, H. G. Nam, R. N. Zare, Microdroplet fusion mass spectrometry for fast reaction kinetics. *Proc. Natl. Acad. Sci. U.S.A.* **112**, 3898–3903 (2015).
31. L. M. Fidalgo *et al.*, Coupling microdroplet microreactors with mass spectrometry: Reading the contents of single droplets online. *Angew. Chem. Int. Ed.* **48**, 3665–3668 (2009).
32. M. Girod, E. Moyano, D. I. Campbell, R. Graham Cooks, Accelerated bimolecular reactions in microdroplets studied by desorption electrospray ionization mass spectrometry. *Chem. Sci.* **2**, 501–510 (2011).
33. T. Rainer, R. Eidelpe, M. Tollinger, T. Müller, Microdroplet mass spectrometry enables extremely accelerated pepsin digestion of proteins. *J. Am. Soc. Mass Spectrom.* **32**, 1841–1845 (2021).
34. M. Ahmadi, M. Á. Aguirre, A. Canals, “Chapter 1—An introduction to nebulizers” in *Analytical Nebulizers*, A. Canals, M. Á. Aguirre, M. Ahmadi, Eds. (Elsevier, 2023), pp. 3–10.
35. R. D. Gurpur, E. R. Prabhu, M. W. Williams, P. L. Urban, Mass spectrometry using electrospray ionization. *Nat. Rev. Methods Primers* **3**, 23 (2023).
36. C. van de Jan *et al.*, Spray techniques: How to optimise spray deposition and minimise spray drift. *Environmentalist* **28**, 9–17 (2008).
37. S. Cheng, S. Chandra, A pneumatic droplet-on-demand generator. *Exp. Fluids* **34**, 755–762 (2003).
38. S. Poozesh, K. Saito, N. K. Akafuah, J. Graña-Otero, Comprehensive examination of a new mechanism to produce small droplets in drop-on-demand inkjet technology. *Appl. Phys. A* **122**, 110 (2016).
39. L. Frenz *et al.*, Droplet-based microreactors for the synthesis of magnetic iron oxide nanoparticles. *Angew. Chem. Int. Ed.* **47**, 6817–6820 (2008).
40. J. C. Vollenbroek *et al.*, Droplet microreactor for high-throughput fluorescence-based measurements of single catalyst particle acidity. *Microsyst. Nanoeng.* **9**, 39 (2023).
41. V. Taly, B. T. Kelly, A. D. Griffiths, Droplets as microreactors for high-throughput biology. *ChemBioChem* **8**, 263–272 (2007).

42. C. T. Riche, E. J. Roberts, M. Gupta, R. L. Brutchey, N. Malmstadt, Flow invariant droplet formation for stable parallel microreactors. *Nat. Commun.* **7**, 10780 (2016).
43. M. S. McPartlan *et al.*, Atmospheric sampling mass spectrometers activate and ionize neutral water microdroplets to MeV energies and up to 200,000+ charges: Implications for water stability and unusual chemistry in microdroplets. *ACS Cent. Sci.* (2025), 10.1021/acscentsci.5c01518.
44. Z. Wei *et al.*, High yield accelerated reactions in nonvolatile microthin films: Chemical derivatization for analysis of single-cell intracellular fluid. *Chem. Sci.* **9**, 7779–7786 (2018).
45. X. Song *et al.*, Clarifying the identity of the m/z 36 ion in water microdroplet mass spectra. *J. Phys. Chem. A* **129**, 4529–4534 (2025).
46. D. Xing *et al.*, Challenges in detecting hydroxyl radicals generated in water droplets with mass spectrometry. *Anal. Chem.* **97**, 7995–8000 (2025).
47. D. Xing *et al.*, Capture of hydroxyl radicals by hydronium cations in water microdroplets. *Angew. Chem. Int. Ed.* **61**, e202207587 (2022).
48. B. Li, X. Gao, D. Xing, X. Zhang, Comparing sprayed water microdroplets with several ionization methods on the capability of ionizing ambient air. *J. Phys. Chem. A* **129**, 7183–7188 (2025).
49. C. Gong *et al.*, Spontaneous reduction-induced degradation of viologen compounds in water microdroplets and its inhibition by host-guest complexation. *J. Am. Chem. Soc.* **144**, 3510–3516 (2022).
50. X. Yuan, D. Zhang, C. Liang, X. Zhang, Spontaneous reduction of transition metal ions by one electron in water microdroplets and the atmospheric implications. *J. Am. Chem. Soc.* **145**, 2800–2805 (2023).
51. Y. Xia, YuXia19/Droplet-on-Demand-Mass-Spectrometry-. Github. <https://github.com/YuXia19/Droplet-on-Demand-Mass-Spectrometry->. Deposited 25 November 2025.